

LETTER TO THE EDITOR

Dense gas tracer scaling relations at kiloparsec scale across nearby galaxies with the ALMA ALMOND and IRAM 30-m EMPIRE surveys

Lukas Neumann^{1,2,*}, María J. Jiménez-Donaire^{3,4}, Adam K. Leroy⁵, Frank Bigiel¹, Antonio Usero³, Jiayi Sun⁶, Eva Schinnerer⁷, Miguel Querejeta³, Sophia K. Stuber⁷, Ivana Bešlić⁸, Ashley Barnes², Jakob den Brok⁹, Yixian Cao¹⁰, Cosima Eibensteiner^{11**}, Hao He¹, Ralf S. Klessen^{12,13,14,15}, Fu-Heng Liang¹⁶, Daizhong Liu¹⁷, Hsi-An Pan¹⁸, and Thomas G. Williams¹⁹

(Affiliations can be found after the references)

Received XX XX, 2024; accepted XX XX, 2024

ABSTRACT

Dense, cold gas is the key ingredient for star formation. Over the last two decades, HCN(1–0) emission has been utilised as the most accessible dense gas tracer to study external galaxies. We present new measurements tracing the relationship between dense gas tracers, bulk molecular gas tracers, and star formation in the ALMA ALMOND survey, the largest sample of resolved (1–2 kpc resolution) HCN maps of galaxies in the local universe ($d < 25$ Mpc). We measure HCN/CO, a line ratio sensitive to the physical density distribution, and SFR/HCN, a proxy for the dense gas star formation efficiency, as a function of molecular gas surface density, stellar mass surface density, and dynamical equilibrium pressure across 31 galaxies, increasing the number of galaxies by a factor of > 3 over the previous largest such study (EMPIRE). HCN/CO increases (slope of ≈ 0.5 and scatter of ≈ 0.2 dex), while SFR/HCN decreases (slope of ≈ -0.6 and scatter of ≈ 0.4 dex) with increasing molecular gas surface density, stellar mass surface density and pressure. Galaxy centres with high stellar mass surface density show a factor of a few higher HCN/CO and lower SFR/HCN compared to the disc average, but both environments follow the same average trend. Our results emphasise that molecular gas properties vary systematically with the galactic environment and demonstrate that the scatter in the Gao-Solomon relation (SFR against HCN) is of physical origin.

Key words. ISM: molecules – Galaxies: ISM – Galaxies: star formation

1. Introduction

Stars form from the coldest, densest substructures within molecular clouds. Higher-critical density molecular lines (“dense gas tracers”) trace this denser subset of molecular gas in contrast to that probed by low-J CO lines. The brightest and most commonly used extragalactic dense gas tracers are HCN(1–0) and HCO⁺(1–0), hereafter HCN and HCO⁺. A nearly linear correlation has been observed between the star formation rate (SFR) and dense gas tracer luminosity across a wide range of scales (e.g., Gao & Solomon 2004; Wu et al. 2010; García-Burillo et al. 2012; Usero et al. 2015; Chen et al. 2017). This has been interpreted to indicate a regulating role for dense gas in the star formation process. This prompts the question “what sets the amount of dense gas?” Moreover, already in these early studies there have been suggestions that the rate of star formation per unit dense gas tracer luminosity or dense gas mass ($\text{SFE}_{\text{dense}} \equiv \text{SFR}/M_{\text{dense}}$) is not universal, but varies from galaxy-to-galaxy and location-to-location (García-Burillo et al. 2012; Usero et al. 2015; Chen et al. 2015).

Recently, the first dense gas tracer mapping surveys that cover whole galaxies have emerged. The IRAM-30m large program EMPIRE¹ (Bigiel et al. 2016; Jiménez-Donaire et al.

2017, 2019) obtained \sim kpc-resolution maps of dense gas tracers (HCN, HCO⁺, HNC(1–0)), and CO isotopologues for nine nearby galaxies. The ALMA ALMOND² survey (Neumann et al. 2023b) used the Morita Atacama Compact Array (ACA) to map HCN, HCO⁺, and CS(2–1) emission from 25 nearby galaxies that overlap the PHANGS–ALMA CO(2–1) survey (Leroy et al. 2021a). Meanwhile, a number of smaller surveys observed dense gas tracers in small samples of 1–4 galaxies (e.g. Tan et al. 2018; Gallagher et al. 2018b,a; Querejeta et al. 2019; Bešlić et al. 2021; Heyer et al. 2022; Neumann et al. 2024; Lin et al. 2024).

These mapping surveys confirmed significant variations in the SFR/HCN and HCN/CO ratios. SFR/HCN serves as a proxy for the star formation efficiency in denser gas. HCN/CO contrasts high and low critical gas density tracers and so probes the physical density distribution. Both quantities correlate with the local stellar and gas surface density, dynamical equilibrium pressure, and other environmental factors. These variations have a regular sense, with denser gas (higher HCN/CO) and lower SFR/HCN in high surface density, high-pressure regions (e.g. Jiménez-Donaire et al. 2019). At face value, this implies an environment-dependent dense gas star formation efficiency and gas density across the discs of star-forming galaxies.

This letter presents new measurements of HCN/CO and SFR/HCN as a function of local conditions for the 25 galaxies in the ALMA ALMOND survey, which is the largest mapping survey of dense gas tracers in galaxy discs. We synthesise AL-

* e-mail: lukas.neumann.astro@gmail.com

** Jansky Fellow of the National Radio Astronomy Observatory

¹ Eight MIXing Receiver (EMIR) Multiline Probe of the Interstellar medium (ISM) Regulating galaxy Evolution; <https://empiresurvey.yourwebsitespace.com>

² ACA Large-sample Mapping Of Nearby galaxies in Dense gas.

MOND with the IRAM 30-m EMPIRE survey, the first large dense gas tracer mapping survey, to present a homogeneously measured set of kiloparsec-resolution scaling relations that connect star formation, dense gas, and total molecular gas to these local environmental quantities for a total of 31 local, spiral galaxies.

2. Data & Methods

We use the HCN data presented in Jiménez-Donaire et al. (2019, EMPIRE) and Neumann et al. (2023b, ALMOND), which span stellar masses from $8 \times 10^9 M_\odot$ to $1 \times 10^{11} M_\odot$ and SFRs from $0.2 M_\odot \text{ yr}^{-1}$ to $17 M_\odot \text{ yr}^{-1}$. The two data sets are well-matched in sensitivity and resolution (see App. D, median 1.47 kpc, 16-84% range 1.09-1.76 kpc). We convolve all supporting data to the angular resolution of the HCN observations using the PyStructure package³. We sample all maps with a half-beam spaced hexagonal grid and compute the integrated intensities of the HCN and CO lines by integrating over a velocity range determined by the velocity extent of CO emission. The velocity integration mask is built from 4-sigma CO peaks and expanded into adjacent 2-sigma channels. We treat the ratios HCN/CO and SFR/HCN as the quantities of interest and measure how these vary as a function of the molecular gas mass surface density (Σ_{mol}), stellar mass surface density (Σ_\star), and dynamical equilibrium pressure (P_{DE}).

Galaxy sample Table E.1 lists our targets, their integrated properties, survey coverage, and the resolution of the HCN observations. ALMOND and EMPIRE target nearby ($d < 25$ Mpc), $i < 75^\circ$, star-forming ($\text{SFR} \sim 0.2 - 17 M_\odot \text{ yr}^{-1}$) galaxies, which span stellar masses from $8 \times 10^9 M_\odot$ to $1 \times 10^{11} M_\odot$ and SFRs from $0.2 M_\odot \text{ yr}^{-1}$ to $17 M_\odot \text{ yr}^{-1}$. We stress that ALMOND significantly increases the dynamic range of SFR and M_\star (by \sim factor of 2) compared to the previous largest sample (i.e., EMPIRE; see Fig. 1). Combining the surveys yields 31 unique galaxies. NGC 628, 2903, and 4321 overlap between surveys and yield consistent results (see App. D). To avoid duplicates, we employ the ALMOND data for these galaxies.

Star formation rate We estimate kpc-scale SFR and SFR surface density (Σ_{SFR}) following the methodology of the original ALMOND paper (Neumann et al. 2023b), which uses a combination of infrared (IR) ($22 \mu\text{m}$) maps from WISE (Wright et al. 2010) and far-ultraviolet (FUV, 154 nm) maps from GALEX (Martin et al. 2005). These maps are taken from the zOMGS atlas (Leroy et al. 2019) and converted to SFR following their best FUV+ $22\mu\text{m}$ prescription. Although EMPIRE employed *Spitzer* and *Herschel* IR to estimate the SFR, here we adopt the same methodology across EMPIRE and ALMOND, using the FUV+ $22\mu\text{m}$ based SFR maps across the full sample.

Stellar mass We estimate stellar mass surface density (Σ_\star) from *Spitzer* $3.6 \mu\text{m}$ observations (Sheth et al. 2010; Querejeta et al. 2021). We use the dust-corrected maps from Querejeta et al. (2015) and adopt a mass-to-light ratio of $\Upsilon_\star = 0.6 M_\odot L_\odot^{-1}$.

Dynamical equilibrium pressure The dynamical equilibrium pressure (P_{DE}) expresses the total interstellar pressure needed to support a disc in vertical dynamical equilibrium (e.g., see Ostriker & Kim 2022; Schinnerer & Leroy 2024). We estimate P_{DE}

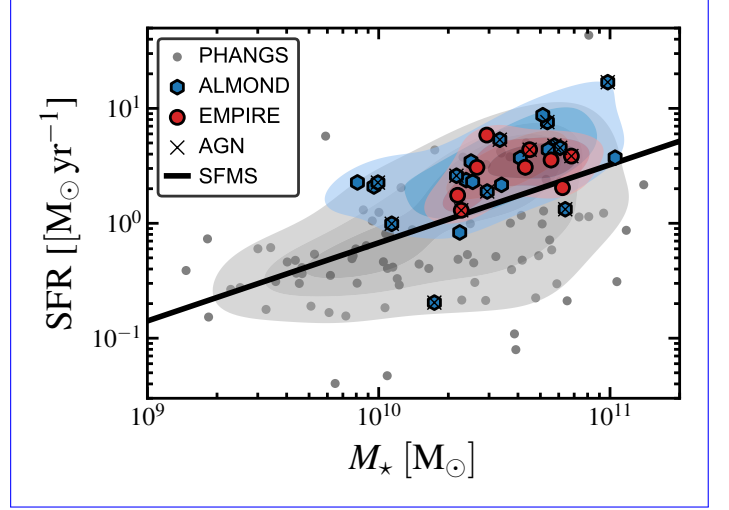


Fig. 1. ALMOND and EMPIRE on the star-forming main sequence (SFMS) of galaxies. Grey shows all galaxies from the PHANGS–ALMA survey (Leroy et al. 2021b). Red and blue markers present galaxies from the EMPIRE (Jiménez-Donaire et al. 2019) and ALMOND surveys (Neumann et al. 2023b), respectively, adopting the same SFR calibration across the merged sample. Contours indicate 25, 50 and 75 percentile areas of the respective samples. The black solid line marks the star-forming main sequence from zOMGS (Leroy et al. 2019). The black squares and crosses indicate the presence of a bar or active galactic nucleus (AGN) in the respective galaxy, taken from Tab. E.1.

by calculating the weight of the ISM in the galaxy potential via:

$$P_{\text{DE}} = \frac{\pi G}{2} \Sigma_{\text{gas}}^2 + \Sigma_{\text{gas}} \sqrt{2G\rho_\star} \sigma_{\text{gas},z}, \quad (1)$$

where $\Sigma_{\text{gas}} = \Sigma_{\text{mol}} + \Sigma_{\text{atom}}$ is the total gas surface density, ρ_\star is the stellar mass volume density, and $\sigma_{\text{gas},z} = 15 \text{ km s}^{-1}$ (e.g. Sun et al. 2018) is the gas velocity dispersion perpendicular to the galactic disc. Computing ρ_\star requires estimates of the stellar scale heights, which are estimated from measured stellar disc scale lengths by assuming a typical disc flattening ratio (see Sun et al. 2020b, 2022, for more details). Estimating P_{DE} additionally requires measurements of the atomic gas content, which have been taken from H I 21-cm line observation (all at similar or higher angular resolution than HCN), available for 25–26 galaxies of our sample (Tab. E.1), hence limiting the analysis of P_{DE} relations to those 25–26 galaxies.

Conversion factors, molecular gas surface density, and dense gas fraction We focus on the ratios HCN/CO and SFR/HCN. For reference we convert them to fiducial physical quantities using fixed conversion factors $\alpha_{\text{CO}} \equiv M_{\text{mol}}/L_{\text{CO}} \equiv \Sigma_{\text{mol}}/W_{\text{CO}}$ and $\alpha_{\text{HCN}} \equiv M_{\text{dense}}/L_{\text{HCN}} \equiv \Sigma_{\text{dense}}/W_{\text{HCN}}$, adopting $\alpha_{\text{CO}}^{\text{fix}} = 4.35 M_\odot \text{ pc}^{-2} (\text{K km s}^{-1})^{-1}$ (Bolatto et al. 2013) and $\alpha_{\text{HCN}} = 15 M_\odot \text{ pc}^{-2} (\text{K km s}^{-1})^{-1}$ (Schinnerer & Leroy 2024). Aside from aiming to remain “close to the observations”, we do this because the environmental dependence of the HCN to dense gas conversion factor, α_{HCN} , remains unclear, with no obvious best prescription and likely significant covariance with α_{CO} (see Usuro et al. 2015).

Nevertheless, to leverage recent progress in understanding α_{CO} variations, we employ a variable α_{CO} (hereafter $\alpha_{\text{CO}}^{\text{var}}$) when considering molecular gas surface density, Σ_{mol} , or dynamical equilibrium pressure (P_{DE} ; see paragraphs below) as indepen-

³ <https://github.com/jdenbrok/PyStructure>

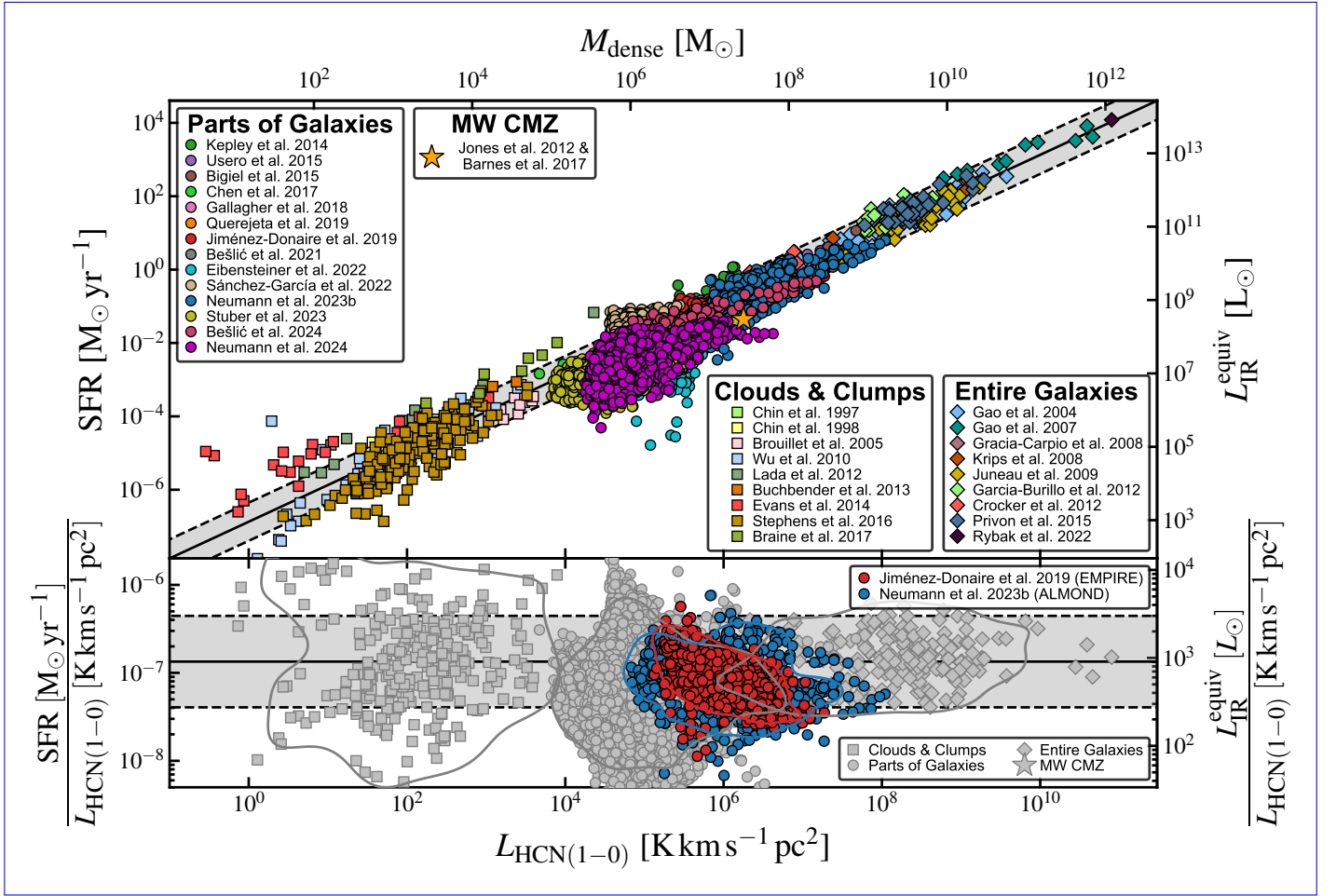


Fig. 2. Gao–Solomon relation. Star formation rate (SFR, top) and SFR/ L_{HCN} (proxy of $\text{SFE}_{\text{dense}}$, bottom) as a function of HCN luminosity, across a literature compilation and the ALMOND (blue circles) and EMPIRE (red circles) surveys. Note that we re-calculate SFR across EMPIRE galaxies using a combination of IR and FUV data (see Sect. 2). Our literature compilation contains HCN observations that include Galactic clumps and clouds (squares), resolved nearby galaxies (circles) and unresolved entire galaxies (diamonds). For more details on the compilation see App. B. The plotted data points show all (3-sigma) detected sightlines. The black solid line shows the median SFR/HCN computed from these data points across all data sets (without duplicates across targets), and the dashed lines mark the 1-sigma scatter (Tab. 1). The bottom panel shows the ratio SFR/HCN as a function of L_{HCN} , grouping the data into the same sub-samples where the 10-percentile density contours of the respective sub-samples are shown. We plot ALMOND and EMPIRE separately, and the blue and red contours present the 10-percentile levels of these surveys.

Table 1. Gao–Solomon relation

Regime	$\log_{10} \text{SFR/HCN}$	$\log_{10} \text{IR/HCN}$	$\log_{10} \tau_{\text{dep}}^{\text{dense}}$	σ
	$[\text{M}_{\odot} \text{yr}^{-1} / (\text{K km s}^{-1} \text{pc}^2)]$	$[\text{L}_{\odot} / (\text{K km s}^{-1} \text{pc}^2)]$	$[\text{yr}]$	
	(16 th , 50 th , 84 th) perc.	(16 th , 50 th , 84 th) perc.	(16 th , 50 th , 84 th) perc.	
Clouds & Clumps	(−7.43, −6.89, −6.27)	(2.40, 2.94, 3.56)	(7.45, 8.07, 8.61)	0.70
Parts of Galaxies	(−7.23, −6.98, −6.65)	(2.60, 2.85, 3.18)	(7.82, 8.16, 8.41)	0.46
Entire Galaxies	(−7.16, −6.85, −6.56)	(2.67, 2.98, 3.27)	(7.74, 8.03, 8.33)	0.27
Combined	(−7.17, −6.87, −6.48)	(2.66, 2.96, 3.35)	(7.66, 8.05, 8.34)	0.52
ALMOND & EMPIRE	(−7.14, −6.84, −6.44)	(2.69, 2.99, 3.39)	(7.62, 8.02, 8.31)	0.35

Notes – Median dense gas ratios across the combined literature sample presented in Fig. 2, including ALMOND and EMPIRE, and for respective sub-samples, including clouds/clumps, resolved and integrated galaxy surveys. The values across the ‘Parts of Galaxies’ studies are computed from unique targets (i.e., Bigiel et al. 2015; Kepley et al. 2014; Jiménez-Donaire et al. 2019; Sánchez-García et al. 2022; Neumann et al. 2023b; Bešlić et al. 2024). The ‘Combined’ measurements are computed from the medians of each respective study. ‘ALMOND & EMPIRE’ results are obtained from the medians of each respective galaxy (i.e. from 31 galaxies) and consider non-detections (in contrast to the other columns, which only consider 3-sigma detected data). All values are displayed on a logarithmic scale. Columns 2 and 3 list the 16th percentiles, medians, and 84th percentiles of $\log_{10} \text{SFR/HCN}$ and $\log_{10} \text{IR/HCN}$. Column 4 displays the dense gas depletion time ($\tau_{\text{dep}}^{\text{dense}}$) in units of years and column 5 the 1-sigma scatter (σ) of the detected HCN data around the median value in units of dex. See App. B regarding the details of the compilation.

dent variables (i.e., on the x -axis). We calculate

$$\left(\frac{\Sigma_{\text{mol}}}{\text{M}_{\odot} \text{pc}^{-2}}\right) = \alpha_{\text{CO}}^{\text{var}} \left(\frac{W_{\text{CO}}}{\text{K km s}^{-1}}\right) \cos(i), \quad (2)$$

adopting the $\alpha_{\text{CO}}^{\text{var}}$ prescription from Schinnerer & Leroy (2024). $\alpha_{\text{CO}}^{\text{var}}$ depends on metallicity and Σ_{\star} . See App. A for more details on the variable conversion factor and line ratio prescriptions, including references to the works synthesised by Schinnerer & Leroy (2024).

When quoting HCN/CO, we cast our results in terms of CO(1–0) and employ the CO(2–1)/CO(1–0) line ratio calibration as a function of Σ_{SFR} to convert PHANGS–ALMA CO(2–1) into CO(1–0) intensities (see App. A). EMPIRE already has CO(1–0) maps.

For both quantities, we provide reference conversions to physical units. We calculate the “dense gas fraction” as the ratio between dense and bulk molecular gas using these fixed conversion factors, $f_{\text{dense}} \equiv M_{\text{dense}}/M_{\text{mol}} \propto \text{HCN}/\text{CO}$:

$$f_{\text{dense}} \approx 3.5 \left(\frac{W_{\text{HCN}}}{\text{K km s}^{-1}}\right) \left(\frac{W_{\text{CO}}}{\text{K km s}^{-1}}\right)^{-1}. \quad (3)$$

We convert SFR/HCN to an approximate star formation efficiency of dense molecular gas, $\text{SFE}_{\text{dense}} \equiv \text{SFR}/M_{\text{dense}}$, via:

$$\left(\frac{\text{SFE}_{\text{dense}}}{\text{yr}^{-1}}\right) \approx 6.7 \times 10^{-2} \left(\frac{\Sigma_{\text{SFR}}}{\text{M}_{\odot} \text{yr}^{-1} \text{pc}^{-2}}\right) \left(\frac{W_{\text{HCN}}}{\text{K km s}^{-1}}\right)^{-1}. \quad (4)$$

~~Gao–Solomon relation. Star formation rate (SFR, top) and SFR/ L_{HCN} (proxy of, bottom) as a function of HCN luminosity, across a literature compilation and the ALMOND (blue circles) and EMPIRE (red circles) surveys. Note that we re-calculate SFR across EMPIRE galaxies using a combination of IR and FUV data (see Sect. 2). Our literature compilation contains HCN observations that include Galactic clumps and clouds (squares), resolved nearby galaxies (circles) and unresolved entire galaxies (diamonds). For more details on the compilation see App. B. The plotted data points show all (3-sigma) detected sightlines. The black solid line shows the median SFR/HCN computed from these data points across all data sets (without duplicates across targets), and the dashed lines mark the 1-sigma scatter (Tab. 1). The bottom panel shows the ratio SFR/HCN as a function of, grouping the data into the same sub-samples where the 10-percentile density contours of the respective sub-samples are shown. We plot ALMOND and EMPIRE separately, and the blue and red contours present the 10-percentile levels of these surveys.~~

3. Results & Discussion

3.1. Gao–Solomon relation

In Fig. 2, we present the “Gao–Solomon” relation (Gao & Solomon 2004), the scaling relationship between SFR and L_{HCN} . We place ALMOND and EMPIRE in the context of a literature compilation that comprises 31 HCN surveys spanning from the Milky Way to the high-redshift universe. This includes observations of individual cores and molecular clouds within the Milky Way and the Local Group, spatially resolved maps of galaxies, and integrated galaxy data. On the x - and y -axes, we indicate both the observed luminosities (HCN and IR) and the inferred

physical quantities (M_{dense} and SFR), assuming linear conversions with fixed conversion factors α_{HCN} and C_{IR} ⁴. ALMOND and EMPIRE form the largest resolved galaxy data set, filling in the large gap in spatial scale, SFR, and L_{HCN} between the integrated galaxy and individual cloud studies.

In the bottom panel of Fig. 2, the y -axis displays the ratio between SFR and L_{HCN} . Across the full literature sample, we find a median SFR/HCN of $1.3 \times 10^{-7} \text{ M}_{\odot} \text{yr}^{-1} (\text{K km s}^{-1} \text{pc}^2)^{-1}$ with a 1-sigma scatter of 0.52 dex consistent with previous literature compilations (e.g., Jiménez-Donaire et al. 2019; Bešlić et al. 2024). We also compute the respective median $\text{SFE}_{\text{dense}}$ values and scatter for the individual sub-samples: clumps and clouds (squares), resolved galaxy observations (circles), and entire galaxies (diamonds). The values, along with the values specifically for ALMOND and EMPIRE, are listed in Tab. 1. Overall, the literature compilation demonstrates that the HCN luminosity is a reasonable predictor of the SFR from cloud to galaxy scale across 10 orders of magnitude. However, at any given HCN luminosity, there is a significant scatter $\sigma \sim 0.5$ dex. Moreover, the scatter increases from large (entire galaxy; $\sigma = 0.27$ dex) to small scales (clouds; $\sigma = 0.70$ dex), suggesting that there are significant variations of $\text{SFE}_{\text{dense}}$ within galaxies (discussed in Sect. 3.2) that average out at integrated galaxy scales.

SFR/HCN can be interpreted, with significant uncertainty due to the uncertain conversion factor, as the rate per unit mass at which dense molecular gas converts into stars. Across the detected sightlines of the full literature sample, we find a median $\text{SFE}_{\text{dense}} \approx 8.9 \times 10^{-9} \text{ yr}^{-1}$, or equivalently, a median dense gas depletion time of $\tau_{\text{dep}}^{\text{dense}} \approx 112 \text{ Myr}$, indicating that the rate of present-day star formation would consume the available dense gas in this time period. For reference, this is ≈ 10 times lower than estimates for $\tau_{\text{dep}}^{\text{mol}}$, the overall molecular gas depletion time in similar samples (Sun et al. 2023). The star formation efficiency per free-fall time, $\epsilon_{\text{ff}}^{\text{dense}} = \text{SFE}_{\text{dense}} \cdot t_{\text{ff}}^{\text{dense}}$, is of theoretical interest (e.g., Krumholz & McKee 2005; Federrath & Klessen 2012) because it captures the efficiency of star formation relative to the timescale expected for gravitational collapse, and so normalizes for density. The free-fall time of the dense molecular gas is computed as $t_{\text{ff}}^{\text{dense}} = 0.8 \text{ Myr}$, assuming that HCN traces gas above a density of $n_{\text{H}_2}^{\text{dense}} \approx 3 \times 10^3 \text{ cm}^{-3}$ (Jones et al. 2023; Bemis et al. 2024). Across the full literature sample, we obtain a median $\epsilon_{\text{ff}}^{\text{dense}} \approx 0.7\%$, which suggests that only 0.7% of the dense molecular gas is converted into stars per gravitational collapse timescale. This demonstrates that even in the dense gas, star formation appears to be an extremely inefficient process.

3.2. Dense gas relations with environment

Figure 2 shows significant scatter in SFR/HCN. Previous works find both SFR/HCN and HCN/CO depend systematically on environmental factors, including stellar mass surface density (Σ_{\star}), molecular gas mass surface density (Σ_{mol}), and interstellar pressure inferred from dynamical equilibrium (P_{DE}) (Usero et al. 2015; Gallagher et al. 2018b; Jiménez-Donaire et al. 2019). The combined ALMOND and EMPIRE samples are ideal to measure these environmental variations. Individual regions follow the overall Gao–Solomon relation and show a comparable scatter to the full literature sample. The resolution of $\sim \text{kiloparsec}$ is, on the one hand, high enough to resolve galaxies into discrete re-

⁴ All data here have observed HCN, but for the y -axis we adopt the best-estimate SFR and convert to equivalent L_{IR} using a constant IR-to-SFR conversion factor, $C_{\text{IR}} = 1.48 \times 10^{-10} \text{ M}_{\odot} \text{yr}^{-1} L_{\odot}^{-1}$ (Murphy et al. 2011).

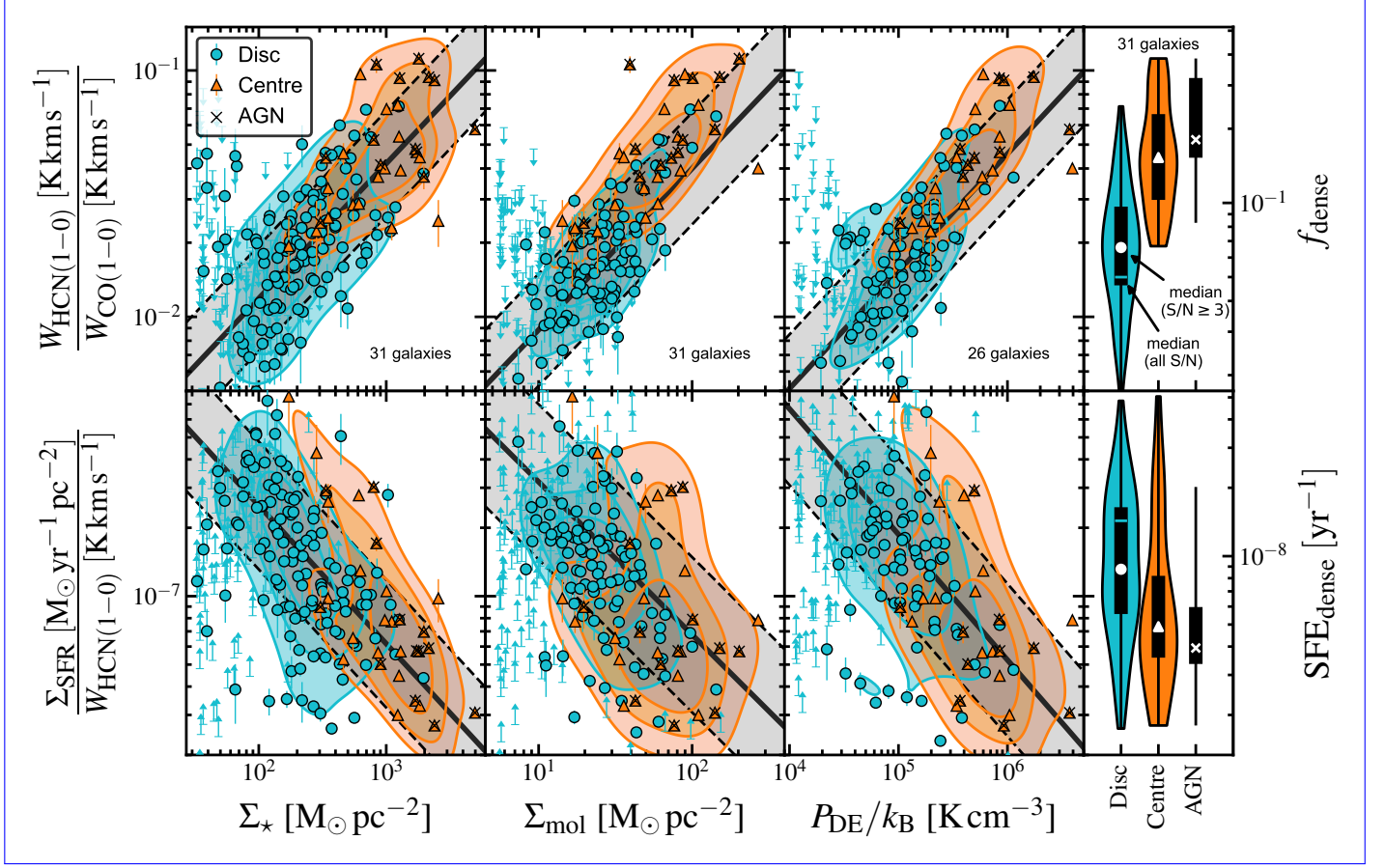


Fig. 3. Dense gas relations with kiloparsec-scale environment. HCN/CO (*top*), a proxy of f_{dense} , and SFR/HCN (*bottom*), a proxy of $\text{SFE}_{\text{dense}}$, as a function of stellar mass surface density (Σ_\star), molecular gas surface density (Σ_{mol}), and dynamical equilibrium pressure (P_{DE}) across 31 galaxies from ALMOND and EMPIRE. The markers denote significant ($S/N \geq 3$) stacked measurements across disc (circle) and centre (triangle) spaxels. The downward and upward pointing arrows denote upper (HCN/CO) and lower limits (SFR/HCN). Filled contours show 25, 50, and 75 percentile kernel density estimates. Across centres, we indicate the presence of an AGN (cross). All relations have been fitted with LinMix taking into account measurement uncertainties and upper/lower limits (parameters in Tab. 2). The black solid line shows the best-fit line and the grey-shaded area indicates the 1-sigma scatter of $S/N \geq 3$ data. The right panels show violin plots of the HCN/CO and SFR/HCN distribution across the respective samples (disc, centre, centre with AGN), where the black bar and white markers indicate the 25th to 75th percentile range and the median, respectively, across the $S/N \geq 3$ data. The vertical cyan lines in the disc violins mark the median computed from all S/N data.

gions like centres, bars and spiral arms and is, on the other hand, coarse enough to average over many individual regions to access the time-averaged mean HCN/CO and SFR/HCN.

In Fig. 3 we use ALMOND and EMPIRE to make the most rigorous measurement to date of the scaling relations relating HCN/CO and SFR/HCN to these environmental factors. For each galaxy we spectrally stack the HCN(1–0) and CO(1–0) lines in bins of Σ_\star , Σ_{mol} , and P_{DE} using PyStacker⁵. We use the CO data, which has much higher signal-to-noise than the HCN to determine the local mean reference velocity for the stacks (see Neumann et al. 2023a, and references therein for details on the spectral stacking methodology; App. C presents the spectral stacks of HCN and CO). For bins in which the stacks do not yield 3-sigma HCN detections, we estimate upper limits for HCN/CO and lower limits for SFR/HCN. We fit the combined set of stacks (including upper limits) for all galaxies using a linear function of the form:

$$\log_{10} Y = b + m \cdot (\log_{10} X - x_0), \quad (5)$$

where $X = \{\Sigma_\star, \Sigma_{\text{mol}}, P_{\text{DE}}\}$ and $Y = \{\text{HCN/CO}, \text{SFR/HCN}\}$ are the x - and y -axis variables, respectively. The slopes and intercepts are denoted as m and b , $x_0 = \{2.4, 1.4, 5.0\}$ is a value close

to median X value. Centering the fit at x_0 minimises the covariance between m and b . The fitting is performed with the linear regression tool LinMix⁶, which takes into account measurement uncertainties and 3-sigma upper (lower) limits on HCN/CO (SFR/HCN) (see e.g. Neumann et al. 2023b, for more details on the fitting routine). The fit parameters are presented in Tab. 2. Note that the range of Σ_\star , Σ_{mol} , and P_{DE} covered by these results corresponds to the molecular gas dominated, inner parts of galaxies, where most stars form.

We measure strong correlations between the stacked HCN/CO and all three quantities and anti-correlations between SFR/HCN and the same quantities (Fig. 3 and Tab. 2). HCN/CO increases, while SFR/HCN decreases with increasing Σ_\star , Σ_{mol} , P_{DE} . The slopes are significant, with both HCN/CO and SFR/HCN changing by ~ 1 dex across our sample. ALMOND and EMPIRE show consistent results despite using different telescopes and using different CO lines (see App. D).

The enhanced HCN/CO in high-surface density, high-pressure environments indicates that deeper gravitational potential and more abundant overall molecular gas lead to the formation of denser molecular clouds. This picture agrees well with the

⁵ <https://github.com/PhangsTeam/PyStacker>

⁶ <https://github.com/jmeyers314/linmix>

Table 2. Dense gas tracer and environment in ALMOND and EMPIRE

$\log_{10}(Y)$	$\log_{10}(X)$	x_0	m (unc.)	b (unc.)	σ	r_{Pearson}
HCN/CO	Σ_\star	2.4	0.55 (0.03)	-1.71 (0.01)	0.21	0.77
	Σ_{mol}	1.4	0.65 (0.05)	-1.79 (0.02)	0.23	0.70
	P_{DE}/k_B	5.0	0.48 (0.04)	-1.81 (0.02)	0.22	0.76
SFR/HCN	Σ_\star	2.4	-0.61 (0.04)	-6.84 (0.02)	0.28	-0.70
	Σ_{mol}	1.4	-0.67 (0.08)	-6.77 (0.02)	0.34	-0.56
	P_{DE}/k_B	5.0	-0.55 (0.05)	-6.73 (0.03)	0.34	-0.66

Notes – Fit parameters obtained via linear regression with LinMix via Equ. 5 to the data shown in Fig. 3. The parameters x_0 , m , b and σ are the x -axis offset, slope, intercept, and scatter of the relation. r_{Pearson} denotes the Pearson correlation coefficient, where all p -values are much smaller than 0.01. Σ_\star and Σ_{mol} are given in units of $\text{M}_\odot \text{pc}^{-2}$; and P_{DE}/k_B in K cm^{-3} .

one that has emerged from high physical resolution CO imaging, which shows that the mean cloud-scale gas surface density and velocity dispersion correlate with these same environmental factors (Sun et al. 2022). In fact, one of the main results from ALMOND has been a good direct correlation between the cloud-scale gas properties and the density-sensitive HCN/CO line ratio (Neumann et al. 2023b). Indeed, the fact that spectroscopic (presented here) and CO imaging results show similar trends as a function of galactic environment provides strong evidence that molecular clouds vary in their physical properties as a function of the galactic environment. The HCN/CO variations that we observe are continuous across the whole range of our sample, with ~ 0.2 dex scatter about the correlation.

SFR/HCN anti-correlates with Σ_\star , Σ_{mol} , and P_{DE} . This anti-correlation is also significant, though the correlation coefficient is weaker, and the data show more residual scatter in SFR/HCN compared to the trends in HCN/CO. At face value, this indicates that the denser molecular gas that effectively emits HCN is less efficiently converted to stars in high surface density, high-pressure parts of galaxies. A popular explanation for this trend has been that HCN-emitting material in these denser environments does not necessarily uniquely correspond to the over-dense, self-gravitating parts of clouds that collapse to form stars (e.g. Krumholz & Thompson 2007; Shetty et al. 2014; Gallagher et al. 2018a; Neumann et al. 2023b; Bemis & Wilson 2023; Bemis et al. 2024).

3.3. Dense gas ratios in galaxy centres

The centres of galaxies often exhibit high Σ_{mol} , Σ_\star , and P_{DE} , hence one expects high HCN/CO and low SFR/HCN in galaxy centres compared to the discs. In Fig. 3, we separately indicate galaxy centres in contrast to the rest of the galaxy. For this exercise, we consider the central kiloparsec-scale, beam size aperture as the centre and refer to the remaining galaxy parts as the disc.

We find that centres typically have high HCN/CO (median of 0.045 compared to disc median of 0.013, which are not consistent within the 1-sigma scatter; Tab. E.2) and low SFR/HCN (median of $7.8 \times 10^{-8} \text{M}_\odot \text{yr}^{-1} \text{pc}^{-2} (\text{K km s}^{-1})^{-1}$ compared to disc median of $1.3 \times 10^{-7} \text{M}_\odot \text{yr}^{-1} \text{pc}^{-2} (\text{K km s}^{-1})^{-1}$, but overlapping 1-sigma intervals). In the following, we base our discussion of the centre-disc comparison on the relations with Σ_\star , which have uncorrelated axes in contrast to the relations with Σ_{mol} and P_{DE} , which depend on the CO line intensity. To first order, centres appear to follow the same average HCN/CO and SFR/HCN

against Σ_\star trend, showing a continuous extension of the disc trends. The higher HCN/CO (lower SFR/HCN) in galaxy centres then simply results from the high Σ_\star (Σ_{mol} , P_{DE}) environment of centres. However, there are some deviations from this simple picture in the SFR/HCN against Σ_\star relation. On the one hand, the disc measurements in intermediate Σ_\star environments ($\Sigma_\star \approx 2 \times 10^2 \text{M}_\odot \text{pc}^{-2} - 1 \times 10^3 \text{M}_\odot \text{pc}^{-2}$) tend to have low SFR/HCN compared to the average trend, while centres show high SFR/HCN across the same Σ_\star range. These deviations could be explained via variations with dynamical environments (e.g. Neumann et al. 2024, found a low SFR/HCN in the galactic bar), but remain speculative due to the coarse, kiloparsec resolution of the ALMOND and EMPIRE observations and hence require higher-resolution observations that resolve these morphological regions.

If taken at face value, the low $\text{SFE}_{\text{dense}}$ in galaxy centres could imply that these environments are typically less efficiently forming stars per unit of dense gas mass, which could be explained by higher gas turbulence in these environments acting against gravitational collapse (e.g., Usero et al. 2015; Neumann et al. 2023b). However, a similarly likely explanation is that HCN might not be a robust tracer of dense gas in galaxy centres (e.g., due to increased optical depth, infrared pumping, e.g. Matsushita et al. 2015, or electron excitation, e.g. Goldsmith & Kauffmann 2018) and potentially trace more of the bulk gas in these high-density regions (see explanation above). Therefore, we might expect that α_{HCN} varies between disc and centre regions. For instance, if one assumes that α_{HCN} variations are driven by optical depth effects and vary similarly to α_{CO} (Teng et al. 2023; Bemis et al. 2024), α_{HCN} would be lower in galaxy centres and thus yield higher $\text{SFE}_{\text{dense}}$ more comparable to disc values.

One might expect that active galactic nuclei (AGN) boost HCN emission (e.g., Goldsmith & Kauffmann 2018; Matsushita et al. 2015), deplete gas (e.g. Ellison et al. 2021), or quench star formation (e.g., Nelson et al. 2019). In Fig. 3, we additionally indicate the presence of an AGN (cross; 14 galaxies) for the galaxy centres and show their median and distribution in the right panels. We find that active centres have 50 % higher HCN/CO and lower SFR, though distributions are similar to those found in non-active galaxies and the differences are not significant at the 1-sigma level. Likely, the variations of dense gas and star formation in AGN-affected regions are not well resolved at the scales ($\sim 1 - 2 \text{kpc}$) probed in this study and require sub-kiloparsec resolution observations.

4. Conclusions

We present the resolved 1–2 kpc resolution dense gas tracer scaling relations for ALMA ALMOND, a survey of HCN emission from 25 star-forming disc galaxies. Combining ALMOND with the IRAM 30-m EMPIRE survey, we measure how HCN/CO and SFR/HCN, observational quantities sensitive to the gas density and star formation efficiency of dense gas, depend on the local stellar and molecular gas mass surface density (Σ_\star and Σ_{SFR}) and the estimated dynamical equilibrium pressure (P_{DE}). Our total sample of 31 resolved galaxies represents a factor of > 3 increase compared to the previous state-of-the-art. HCN/CO correlates with all three environmental measures, showing similar trends to those found for cloud-scale ($\sim 100 \text{pc}$) CO imaging. Our results support the view that the physical state of molecular gas depends on galactic environment. SFR/HCN anti-correlates with surface density and P_{DE} , though these show moderately more scatter than the HCN/CO correlations. This reinforces that the

scatter in the Gao-Solomon relation is physical in origin and that the relation between any specific dense gas tracer and star formation activity appears environment-dependent. While the physical explanations for each of these trends remain subjects of active research, their presence in the data is clear, and ALMA ALMOND + IRAM 30-m EMPIRE provides the best measurement to date in the molecular gas-dominated, star-forming parts of massive disc galaxies.

Acknowledgements. LN acknowledges funding from the Deutsche Forschungsgemeinschaft (DFG, German Research Foundation) - 516405419. AKL gratefully acknowledges support by grants 1653300 and 2205628 from the National Science Foundation, by award JWST-GO-02107.009-A, and by a Humboldt Research Award from the Alexander von Humboldt Foundation. AU acknowledges support from the Spanish grants PGC2018-094671-B-I00, funded by MCIN/AEI/10.13039/501100011033 and by “ERDF A way of making Europe”, and PID2019-108765GB-I00, funded by MCIN/AEI/10.13039/501100011033. [RSK acknowledges financial support via the ERC Synergy Grant “ECOGAL” \(project ID 855130\), via the Heidelberg Cluster of Excellence \(EXC 2181 - 390900948\) “STRUCTURES”, and via the BMWK project “MAINN” \(funding ID 50002206\). RSK also thanks the 2024/25 Class of Radcliffe Fellows for highly interesting and stimulating discussions.](#) FHL gratefully acknowledges funding from the European Research Council’s starting grant ERC StG-101077573 (“ISM-METALS”). HAP acknowledges support from the National Science and Technology Council of Taiwan under grant 110-2112-M-032-020-MY3. This paper makes use of the following ALMA data, which have been processed as part of the ALMOND and PHANGS-ALMA surveys:

ADS/JAO.ALMA#2012.1.00650.S,
ADS/JAO.ALMA#2013.1.01161.S,
ADS/JAO.ALMA#2015.1.00925.S,
ADS/JAO.ALMA#2015.1.00956.S,
ADS/JAO.ALMA#2017.1.00230.S,
ADS/JAO.ALMA#2017.1.00392.S,
ADS/JAO.ALMA#2017.1.00766.S,
ADS/JAO.ALMA#2017.1.00815.S,
ADS/JAO.ALMA#2017.1.00886.L,
ADS/JAO.ALMA#2018.1.01171.S,
ADS/JAO.ALMA#2018.1.01651.S,
ADS/JAO.ALMA#2018.A.00062.S,
ADS/JAO.ALMA#2019.2.00134.S,
ADS/JAO.ALMA#2021.1.00740.S,
ALMA is a partnership of ESO (representing its member states), NSF (USA), and NINS (Japan), together with NRC (Canada), NSC and ASIAA (Taiwan), and KASI (Republic of Korea), in cooperation with the Republic of Chile. The Joint ALMA Observatory is operated by ESO, AUI/NRAO, and NAOJ. The National Radio Astronomy Observatory (NRAO) is a facility of the National Science Foundation operated under cooperative agreement by Associated Universities, Inc. This work makes use of data products from the *Wide-field Infrared Survey Explorer* (WISE), which is a joint project of the University of California, Los Angeles, and the Jet Propulsion Laboratory/California Institute of Technology, funded by NASA. This work is based in part on observations made with the *Galaxy Evolution Explorer* (GALEX). GALEX is a NASA Small Explorer, whose mission was developed in cooperation with the Centre National d’Etudes Spatiales (CNES) of France and the Korean Ministry of Science and Technology. GALEX is operated for NASA by the California Institute of Technology under NASA contract NAS5-98034.

Data availability

The HCN and CO data products used in this paper are publicly available via [https://www.iram.fr/ILPA/LP015/\(EMPIRE\)](https://www.iram.fr/ILPA/LP015/(EMPIRE)), <https://www.canfar.net/storage/list/phangs/RELEASES/ALMOND/> (ALMOND), and <https://www.canfar.net/storage/list/phangs/RELEASES/PHANGS-ALMA/> (PHANGS-ALMA).

References

Anand, G. S., Lee, J. C., Van Dyk, S. D., et al. 2021, *MNRAS*, 501, 3621
Barnes, A. T., Longmore, S. N., Battersby, C., et al. 2017, *MNRAS*, 469, 2263
Bemis, A. R. & Wilson, C. D. 2023, *ApJ*, 945, 42
Bemis, A. R., Wilson, C. D., Sharda, P., Roberts, I. D., & He, H. 2024, *arXiv e-prints*, arXiv:2410.00243

Bešlić, I., Barnes, A. T., Bigiel, F., et al. 2024, *A&A*, 689, A122
Bešlić, I., Barnes, A. T., Bigiel, F., et al. 2021, *MNRAS*, 506, 963
Bigiel, F., Leroy, A. K., Blitz, L., et al. 2015, *ApJ*, 815, 103
Bigiel, F., Leroy, A. K., Jiménez-Donaire, M. J., et al. 2016, *ApJ*, 822, L26
Bolatto, A. D., Wolfire, M., & Leroy, A. K. 2013, *ARA&A*, 51, 207
Braine, J., Shimajiri, Y., André, P., et al. 2017, *A&A*, 597, A44
Brouillet, N., Muller, S., Herpin, F., Braine, J., & Jacq, T. 2005, *A&A*, 429, 153
Buchbender, C., Kramer, C., Gonzalez-Garcia, M., et al. 2013, *A&A*, 549, A17
Chen, H., Braine, J., Gao, Y., Koda, J., & Gu, Q. 2017, *ApJ*, 836, 101
Chen, H., Gao, Y., Braine, J., & Gu, Q. 2015, *ApJ*, 810, 140
Chin, Y. N., Henkel, C., Millar, T. J., Whiteoak, J. B., & Marx-Zimmer, M. 1998, *A&A*, 330, 901
Chin, Y. N., Henkel, C., Whiteoak, J. B., et al. 1997, *A&A*, 317, 548
Chung, A., van Gorkom, J. H., Kenney, J. D. P., Crowl, H., & Vollmer, B. 2009, *AJ*, 138, 1741
Crocker, A., Krips, M., Bureau, M., et al. 2012, *MNRAS*, 421, 1298
de Blok, W. J. G., Healy, J., Maccagni, F. M., et al. 2024, *A&A*, 688, A109
den Brok, J. S., Chatzigiannakis, D., Bigiel, F., et al. 2021, *MNRAS*[arXiv:2103.10442]
Eibensteiner, C., Barnes, A. T., Bigiel, F., et al. 2022, *A&A*, 659, A173
Eibensteiner, C., Sun, J., Bigiel, F., et al. 2024, *A&A*, 691, A163
Ellison, S. L., Wong, T., Sánchez, S. F., et al. 2021, *MNRAS*, 505, L46
Evans, Neal J., I., Heiderman, A., & Vutisalchavakul, N. 2014, *ApJ*, 782, 114
Federrath, C. & Klessen, R. S. 2012, *ApJ*, 761, 156
Gallagher, M. J., Leroy, A. K., Bigiel, F., et al. 2018a, *ApJ*, 868, L38
Gallagher, M. J., Leroy, A. K., Bigiel, F., et al. 2018b, *ApJ*, 858, 90
Gao, Y., Carilli, C. L., Solomon, P. M., & Vanden Bout, P. A. 2007, *ApJ*, 660, L93
Gao, Y. & Solomon, P. M. 2004, *ApJ*, 606, 271
García-Burillo, S., Usero, A., Alonso-Herrero, A., et al. 2012, *A&A*, 539, A8
Goldsmith, P. & Kauffmann, J. 2018, in *American Astronomical Society Meeting Abstracts*, Vol. 231, American Astronomical Society Meeting Abstracts #231, 130.06
Graciá-Carpio, J., García-Burillo, S., Planesas, P., Fuente, A., & Usero, A. 2008, *A&A*, 479, 703
Herrera-Endoqui, M., Díaz-García, S., Laurikainen, E., & Salo, H. 2015, *A&A*, 582, A86
Heyer, M., Gregg, B., Calzetti, D., et al. 2022, *ApJ*, 930, 170
Jiménez-Donaire, M. J., Bigiel, F., Leroy, A. K., et al. 2017, *MNRAS*, 466, 49
Jiménez-Donaire, M. J., Bigiel, F., Leroy, A. K., et al. 2019, *ApJ*, 880, 127
Jones, G. H., Clark, P. C., Glover, S. C. O., & Hacar, A. 2023, *MNRAS*, 520, 1005
Jones, P. A., Burton, M. G., Cunningham, M. R., et al. 2012, *MNRAS*, 419, 2961
Juneau, S., Narayanan, D. T., Moustakas, J., et al. 2009, *ApJ*, 707, 1217
Kepley, A. A., Leroy, A. K., Frayer, D., et al. 2014, *ApJ*, 780, L13
Krips, M., Neri, R., García-Burillo, S., et al. 2008, *ApJ*, 677, 262
Krumholz, M. R. & McKee, C. F. 2005, *ApJ*, 630, 250
Krumholz, M. R. & Thompson, T. A. 2007, *ApJ*, 669, 289
Lada, C. J., Forbrich, J., Lombardi, M., & Alves, J. F. 2012, *ApJ*, 745, 190
Lang, P., Meidt, S. E., Rosolowsky, E., et al. 2020, *ApJ*, 897, 122
Leroy, A. K., Hughes, A., Liu, D., et al. 2021a, *ApJS*, 255, 19
Leroy, A. K., Rosolowsky, E., Usero, A., et al. 2022, *ApJ*, 927, 149
Leroy, A. K., Sandstrom, K. M., Lang, D., et al. 2019, *ApJS*, 244, 24
Leroy, A. K., Schinnerer, E., Hughes, A., et al. 2021b, *ApJS*, 257, 43
Lin, L., Pan, H.-A., Ellison, S. L., et al. 2024, *ApJ*, 963, 115
Martin, D. C., Fanson, J., Schiminovich, D., et al. 2005, *ApJ*, 619, L1
Matsushita, S., Trung, D.-V., Boone, F., et al. 2015, *Publication of Korean Astronomical Society*, 30, 439
Murphy, E. J., Condon, J. J., Schinnerer, E., et al. 2011, *ApJ*, 737, 67
Nelson, D., Pillepich, A., Springel, V., et al. 2019, *MNRAS*, 490, 3234
Neumann, L., Bigiel, F., Barnes, A. T., et al. 2024, *arXiv e-prints*, arXiv:2406.12025
Neumann, L., den Brok, J. S., Bigiel, F., et al. 2023a, *A&A*, 675, A104
Neumann, L., Gallagher, M. J., Bigiel, F., et al. 2023b, *MNRAS*, 521, 3348
Ostriker, E. C. & Kim, C.-G. 2022, *ApJ*, 936, 137
Privon, G. C., Herrero-Illana, R., Evans, A. S., et al. 2015, *ApJ*, 814, 39
Querejeta, M., Meidt, S. E., Schinnerer, E., et al. 2015, *ApJS*, 219, 5
Querejeta, M., Schinnerer, E., Meidt, S., et al. 2021, *A&A*, 656, A133
Querejeta, M., Schinnerer, E., Schrubba, A., et al. 2019, *A&A*, 625, A19
Rybak, M., Hodge, J. A., Greve, T. R., et al. 2022, *A&A*, 667, A70
Sánchez, S. F., Barrera-Ballesteros, J. K., López-Cobá, C., et al. 2019, *MNRAS*, 484, 3042
Sánchez, S. F., Rosales-Ortega, F. F., Iglesias-Páramo, J., et al. 2014, *A&A*, 563, A49
Sánchez-García, M., García-Burillo, S., Pereira-Santaella, M., et al. 2022, *A&A*, 660, A83
Schinnerer, E. & Leroy, A. K. 2024, *arXiv e-prints*, arXiv:2403.19843
Schinnerer, E., Meidt, S. E., Pety, J., et al. 2013, *ApJ*, 779, 42
Sheth, K., Regan, M., Hinz, J. L., et al. 2010, *PASP*, 122, 1397
Shetty, R., Clark, P. C., & Klessen, R. S. 2014, *MNRAS*, 442, 2208

- Stephens, I. W., Jackson, J. M., Whitaker, J. S., et al. 2016, ApJ, 824, 29
- Stuber, S. K., Pety, J., Schinnerer, E., et al. 2023, A&A, 680, L20
- Sun, J., Leroy, A. K., Ostriker, E. C., et al. 2020a, ApJ, 892, 148
- Sun, J., Leroy, A. K., Ostriker, E. C., et al. 2023, ApJ, 945, L19
- Sun, J., Leroy, A. K., Rosolowsky, E., et al. 2022, AJ, 164, 43
- Sun, J., Leroy, A. K., Schinnerer, E., et al. 2020b, ApJ, 901, L8
- Sun, J., Leroy, A. K., Schrubba, A., et al. 2018, ApJ, 860, 172
- Tan, Q.-H., Gao, Y., Zhang, Z.-Y., et al. 2018, ApJ, 860, 165
- Teng, Y.-H., Sandstrom, K. M., Sun, J., et al. 2023, ApJ, 950, 119
- Usero, A., Leroy, A. K., Walter, F., et al. 2015, AJ, 150, 115
- Véron-Cetty, M. P. & Véron, P. 2010, A&A, 518, A10
- Walter, F., Brinks, E., de Blok, W. J. G., et al. 2008, AJ, 136, 2563
- Wright, E. L., Eisenhardt, P. R. M., Mainzer, A. K., et al. 2010, AJ, 140, 1868
- Wu, J., Evans, Neal J., I., Shirley, Y. L., & Knez, C. 2010, ApJS, 188, 313

-
- ¹ Argelander-Institut für Astronomie, Universität Bonn, Auf dem Hügel 71, 53121 Bonn, Germany
- ² [European Southern Observatory \(ESO\), Karl-Schwarzschild-Straße 2, 85748 Garching, Germany](#)
- ³ Observatorio Astronómico Nacional (IGN), C/ Alfonso XII, 3, E-28014 Madrid, Spain
- ⁴ Centro de Desarrollos Tecnológicos, Observatorio de Yebes (IGN), 19141 Yebes, Guadalajara, Spain
- ⁵ Department of Astronomy, The Ohio State University, 140 West 18th Ave, Columbus, OH 43210, USA
- ⁶ Department of Astrophysical Sciences, Princeton University, 4 Ivy Lane, Princeton, NJ 08544, USA
- ⁷ Max Planck Institute for Astronomy, Königstuhl 17, 69117 Heidelberg, Germany
- ⁸ LERMA, Observatoire de Paris, PSL Research University, CNRS, Sorbonne Universités, 75014 Paris, France
- ⁹ ~~European Southern Observatory (ESO), Karl-Schwarzschild-Straße 2, 85748 Garching, Germany~~ Center for Astrophysics | Harvard & Smithsonian, 60 Garden St., 02138 Cambridge, MA, USA
- ¹⁰ Max-Planck-Institut für Extraterrestrische Physik (MPE), Giessenbachstr. 1, D-85748 Garching, Germany
- ¹¹ National Radio Astronomy Observatory, 520 Edgemont Road, Charlottesville, VA 22903, USA
- ¹² Universität Heidelberg, Zentrum für Astronomie, Institut für Theoretische Astrophysik, Albert-Ueberle-Str. 2, 69120 Heidelberg, Germany
- ¹³ Universität Heidelberg, Interdisziplinäres Zentrum für Wissenschaftliches Rechnen, Im Neuenheimer Feld 225, 69120 Heidelberg, Germany
- ¹⁴ Harvard-Smithsonian Center for Astrophysics, 60 Garden Street, Cambridge, MA 02138, U.S.A.
- ¹⁵ [Elizabeth S. and Richard M. Cashin Fellow at the Radcliffe Institute for Advanced Studies at Harvard University, 10 Garden Street, Cambridge, MA 02138, USA](#)
- ¹⁶ Astronomisches Rechen-Institut, Zentrum für Astronomie der Universität Heidelberg, Mönchhofstraße 12-14, D-69120 Heidelberg, Germany
- ¹⁷ Purple Mountain Observatory, Chinese Academy of Sciences, 10 Yuanhua Road, Nanjing 210023, China
- ¹⁸ Department of Physics, Tamkang University, No.151, Yingzhuan Road, Tamsui District, New Taipei City 251301, Taiwan
- ¹⁹ Sub-department of Astrophysics, Department of Physics, University of Oxford, Keble Road, Oxford OX1 3RH, UK

Appendix A: Conversion factors

For EMPIRE, we use the CO(1 – 0) maps obtained as part of the survey. For ALMOND, we use PHANGS–ALMA CO(2 – 1) maps, which we convert to an equivalent CO(1 – 0) intensity before applying α_{CO} . To do this, we estimate a line ratio, R_{21} , based on the local SFR surface density (Σ_{SFR}) following [den Brok et al. \(2021\)](#); [Leroy et al. \(2022\)](#); [Schinnerer & Leroy \(2024\)](#):

$$R_{21} = \frac{\text{CO}(2-1)}{\text{CO}(1-0)} = 0.65 \left(\frac{\Sigma_{\text{SFR}}}{1.8 \times 10^{-2} \text{ M}_{\odot} \text{ yr}^{-1} \text{ kpc}^{-2}} \right)^{0.125}, \quad (\text{A.1})$$

with minimum R_{21} of 0.35 and maximum 1.0. Then we scale the CO(2 – 1) intensity by R_{21}^{-1} to present our results in terms of CO(1 – 0) intensity.

To compute Σ_{mol} and P_{DE} , we adopt the variable α_{CO} prescription from [Schinnerer & Leroy \(2024\)](#), their table 1), which accounts for variations with metallicity (Z ; Z_{\odot} is the solar metallicity) and stellar mass surface density (Σ_{\star}):

$$\alpha_{\text{CO}}^{\text{var}} = \alpha_{\text{CO}}^{\text{fix}} \left(\frac{Z}{Z_{\odot}} \right)^{-1.5} \left(\frac{\max(\Sigma_{\star}, 100 \text{ M}_{\odot} \text{ pc}^{-2})}{100 \text{ M}_{\odot} \text{ pc}^{-2}} \right)^{-0.25}. \quad (\text{A.2})$$

Stellar mass maps are inferred from *Spitzer* 3.6 μm observations as explained in Sect. 2. Metallicities are estimated based on simple scaling relations, following [Sun et al. \(2020a\)](#). These use a global mass-metallicity relation ([Sánchez et al. 2019](#)) and employ a radial metallicity relation with a fixed gradient of -0.1 dex normalised by the effective radius of each galaxy ([Sánchez et al. 2014](#)).

Appendix B: Dense gas literature

In Fig. 2, we present a literature compilation of HCN surveys from local parsec scale over resolved, kiloparsec scale, to unresolved, entire galaxy observations. The cloud- and clump-scale measurements are taken from observations within the Milky Way ([Wu et al. 2010](#); [Lada et al. 2012](#); [Evans et al. 2014](#); [Stephens et al. 2016](#)), the CMZ ([Jones et al. 2012](#); [Barnes et al. 2017](#)) and the Local Group, i.e. LMC/SMC ([Chin et al. 1997, 1998](#)), M31 ([Brouillet et al. 2005](#)), M33 ([Buchbender et al. 2013](#)), low-metallicity local group galaxies ([Braine et al. 2017](#)). Resolved galaxy observations, typically from nearby galaxies at 100 pc to 2 kiloparsec scales, include M82 ([Kepley et al. 2014](#)), M51 ([Usero et al. 2015](#); [Chen et al. 2017](#); [Querejeta et al. 2019](#); [Stuber et al. 2023](#)), NGC 4038/39 ([Bigiel et al. 2015](#)), NGC 3351, NGC 3627, NGC 4254, NGC 4321, NGC 5194 ([Gallagher et al. 2018b](#)), NGC 3627 ([Bešlić et al. 2021](#)), NGC 1068 ([Sánchez-García et al. 2022](#)), NGC 6946 ([Eibensteiner et al. 2022](#)), NGC 4321 ([Neumann et al. 2024](#)), NGC 253 ([Bešlić et al. 2024](#)), and the two larger-sample surveys EMPIRE (nine galaxies; [Jiménez-Donaire et al. 2019](#)) and ALMOND (25 galaxies; [Neumann et al. 2023b](#)). Integrated-galaxy data cover LIRG/ULIRG and AGN galaxies ([Krips et al. 2008](#); [Graciá-Carpio et al. 2008](#); [Juneau et al. 2009](#); [García-Burillo et al. 2012](#); [Privon et al. 2015](#)), early-type galaxies ([Crocker et al. 2012](#)), and high-redshift galaxies ([Gao et al. 2007](#); [Rybak et al. 2022](#)).

Appendix C: Spectral stacking of HCN and CO

We compute spectral stacks of HCN(1 – 0) and CO(1 – 0) line emission in bins of stellar mass surface density, Σ_{\star} , molecular gas surface density, Σ_{mol} , and dynamical equilibrium pressure,

P_{DE} , across the merged sample of 31 galaxies studied in this work. For the ALMOND sample, the CO(2 – 1) intensities from PHANGS–ALMA are first converted into CO(1 – 0) intensities using the line ratio calibration from Sect. A. We note, however, that this has no effect on the stacking procedure. We stack in logarithmic bins for each galaxy individually, selecting ten bins from a fixed minimum ($\Sigma_{\star} = 3 \times 10^1 \text{ M}_{\odot} \text{ pc}^{-2}$, $\Sigma_{\text{mol}} = 5 \text{ M}_{\odot} \text{ pc}^{-2}$, $P_{\text{DE}} = 1 \times 10^4 \text{ k}_{\text{B}} \text{ K cm}^{-3}$) to the maximum value of each galaxy. For the centres versus disc HCN scaling relations (Fig. 3), we exclude the centres from the stacking and stacks across the remaining sightlines adopting nine bins. Figure C.1 shows exemplary spectral stacks of HCN(1 – 0) and CO(1 – 0) as a function of Σ_{\star} across the galaxy NGC 4321.

Appendix D: EMPIRE vs ALMOND

There are three galaxies (i.e. NGC 628, NGC 2903, NGC 4321) that have been mapped in dense gas tracers (e.g. HCN(1 – 0)) by both surveys, EMPIRE, using the IRAM 30 m, and ALMOND, using the ACA at similar spectral (a few km s^{-1}) and angular resolution (a few tenths of arcseconds) and sensitivity (a few mK). In Figures D.1 to D.3, we compare the HCN(1 – 0) data from both surveys. We homogenise the two data sets by convolving to the best common spectral (i.e. 10 km s^{-1}) and spatial (i.e. $33''$) resolution and reproject to the same half-beam size hexagonal pixel grid.

Fig. Figure D.1 shows average HCN(1 – 0) spectra computed across all sightlines within 5 kpc from the galactic centre. We additional overlay CO(2 – 1) average spectra obtained from PHANGS–ALMA ([Leroy et al. 2021b](#)), to indicate molecular line emission from a highly significant tracer. This line has been used to infer the velocity-integration window from which we compute HCN(1 – 0) integrated intensities of $41.6 \pm 7.3 \text{ K km s}^{-1}$, $39.5 \pm 10.7 \text{ K km s}^{-1}$ in NGC 628, $427.8 \pm 47.5 \text{ K km s}^{-1}$, $495.7 \pm 143.5 \text{ K km s}^{-1}$ in NGC 2903, and $475.0 \pm 34.6 \text{ K km s}^{-1}$, $570.2 \pm 84.8 \text{ K km s}^{-1}$ in NGC 4321 from ALMOND and EMPIRE, respectively. The average spectra show similar shape and amplitude, demonstrating little to no bias between ALMOND and EMPIRE observations. The integrated line intensities yield consistent values within their uncertainties. The largest deviations are observed at large velocity offsets from the galaxies' systemic velocities, potentially linked to poor baseline subtraction.

Fig. Figures D.2 and D.3 present a voxel-by-voxel, or pixel-by-pixel comparison between the ALMOND and EMPIRE HCN(1 – 0) brightness temperatures (ppv cube) and integrated intensities (moment-0 map). We find that brightness temperatures and integrated intensities agree well between ALMOND and EMPIRE in all galaxies (deviations $\leq 50\%$ across most detected sightlines) and show little bias ($\leq 10\%$ on average across all data). At lower integrated intensities ($\lesssim 10^{-1} \text{ K km s}^{-1}$), EMPIRE yields moderately larger values than ALMOND, which could indicate differences in the calibration and data reduction pipelines.

The comparison between ALMOND and EMPIRE demonstrated that both data sets yield consistent HCN(1 – 0) intensities and subsequent data products. In this work, we employ the ALMOND data for the three galaxies NGC 628, NGC 2903, NGC 4321, due to the slightly better angular resolution and sensitivity of the ALMOND survey.

Figure D.4 shows the HCN/CO and SFR/HCN versus Σ_{\star} , Σ_{mol} , and P_{DE} scaling relations across ALMOND (blue hexagons) and EMPIRE (red circles) at kiloparsec resolution. Our best-fit relations are similar, though slightly steeper, to those

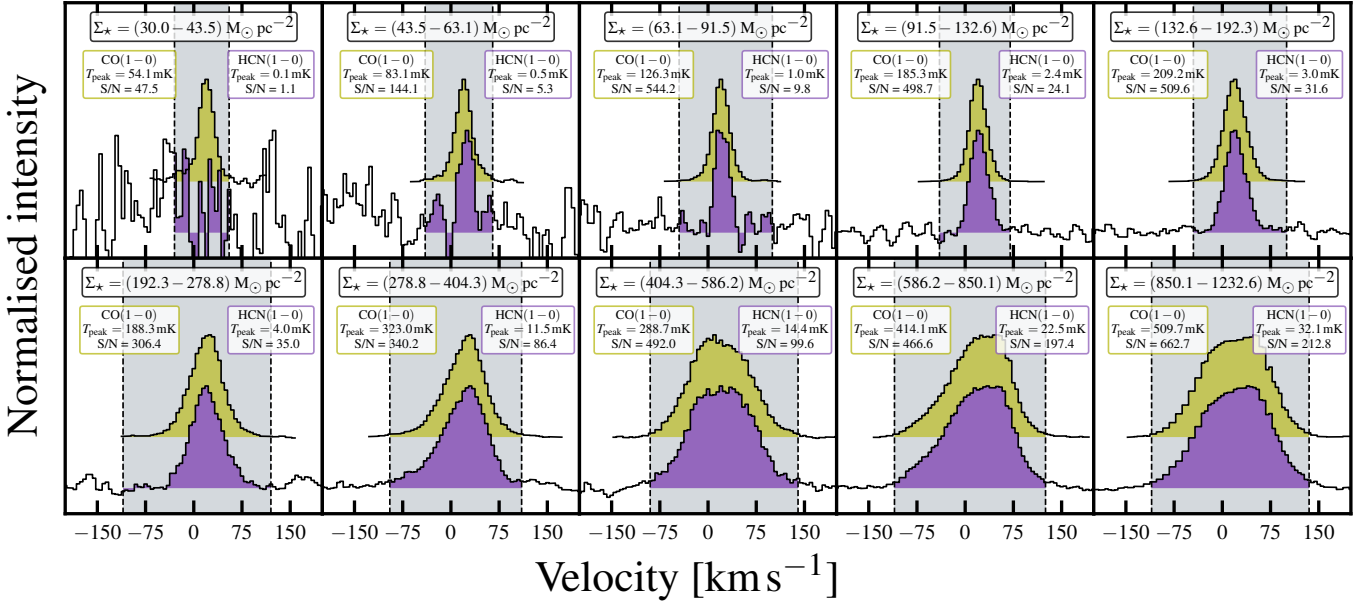


Fig. C.1. Spectral stacks of CO (olive) and HCN (purple) across NGC 4321 in logarithmically-spaced bins of Σ_* . The grey-shaded area indicates the velocity-integration window applied to compute the integrated intensities of the stacked spectra. The labelled boxes show the peak intensity and S/N of the integrated intensities of CO and HCN, respectively, for each stacked spectrum.

reported by Jiménez-Donaire et al. (2019) but are now measured for a larger and more diverse sample of galaxies. The steeper slopes have two reasons: a) the ALMOND sample shows steeper trends, and (b) the inclusion of non-detections into the fitting routines yields $\sim 10\%$ steeper slopes. We observe a larger scatter across the full sample of 31 galaxies compared to the nine EMPIRE galaxies alone, suggesting that the more diverse sample captures a wider range of conditions not captured by the simple scaling relations.

Appendix E: Additional figures/tables

Table E.1 presents the combined galaxy sample composed of 31 galaxies from the EMPIRE and ALMOND surveys, along with their coordinates and global properties.

Figure 1 shows the distribution of galaxies in the SFR against plane across PHANGS, EMPIRE and ALMOND galaxies. The two dense-gas surveys (EMPIRE and ALMOND) utilised in this study encompass massive, actively star-forming galaxies with high SFR, mostly lying above the star-forming main sequence.

ALMOND and EMPIRE on the star-forming main sequence (SFMS) of galaxies. Grey shows all galaxies from the PHANGS ALMA survey (Leroy et al. 2021b). Red and blue markers present galaxies from the EMPIRE (Jiménez-Donaire et al. 2019) and ALMOND (Neumann et al. 2023b), respectively, adopting the same SFR calibration across the merged sample. Contours indicate 25, 50 and 75 percentile areas of the respective samples. The black solid line marks the star-forming main sequence from zOMGS (Leroy et al. 2019). The black squares and crosses indicate the presence of a bar or active galactic nucleus (AGN) in the respective galaxy, taken from Tab. E.1.

Table 1 lists the median and 1-sigma percentile ranges of SFR/HCN, IR/HCN, Σ_* , and its 1-sigma scatter across the literature compilations and respective sub-samples.

Gao-Solomon relation Notes Median dense gas ratios across the combined literature sample presented

in Fig. 2, including ALMOND and EMPIRE, and for respective sub-samples, including clouds/clumps, resolved and integrated galaxy surveys. The values across the ‘Parts of Galaxies’ studies are computed from unique targets (i.e., Bigiel et al. 2015; Kepley et al. 2014; Jiménez-Donaire et al. 2019; ...). The ‘Combined’ measurements are computed from the medians of each respective study. ‘ALMOND & EMPIRE’ results are obtained from the medians of each respective galaxy (i.e. from 31 galaxies) and consider non-detections (in contrast to the other columns, which only consider 3-sigma detected data). All values are displayed on a logarithmic scale. Columns 2 and 3 list the 16th percentiles, medians, and 84th percentiles of \log_{10} SFR/HCN and \log_{10} IR/HCN. Columns 4 and 5 display the median dense gas depletion time (τ) and dense gas star formation efficiency per free-fall time (ϵ), assuming HCN traces gas above $n_{\text{H}_2}^{\text{dense}} \approx 3 \times 10^3 \text{ cm}^{-3}$ and using $\alpha_{\text{HCN}} = 15 \text{ M}_{\odot} \text{ pc}^{-2} (\text{K km s}^{-1})^{-1}$. Column 6 shows the 1-sigma scatter (σ) in dex of the detected HCN data around the median value. See App. B regarding the details of the compilation.

Table 2 shows the best-fit parameters of the HCN/CO and SFR/HCN versus Σ_* , and scaling relations shown in Fig. 3.

Dense gas tracer and environment in ALMOND and EMPIRE $\log_{10}(Y) \log_{10}(X) x_0 m (\text{unc.}) b (\text{unc.}) \sigma r_{\text{Pearson}}$
 2.4 0.55 (0.03) -1.71 (0.01) 0.21 0.77 1.4 0.65 (0.05) -1.79 (0.02)
 0.23 0.70 5.0 0.48 (0.04) -1.81 (0.02) 0.22 0.76 2.4 -0.61 (0.04)
 -6.84 (0.02) 0.28 -0.70 1.4 -0.67 (0.08) -6.77 (0.02)
 0.34 -0.56 5.0 -0.55 (0.05) -6.73 (0.03) 0.34 -0.66 Notes
 Fit parameters obtained via linear regression with LinMix via Equ. 5 to the data shown in Fig. 3. The parameters x_0, m, b and σ are the x -axis offset, slope, intercept, and scatter of the relation. r_{Pearson} denotes the Pearson correlation coefficient, where all p -values are much smaller than 0.01, and are given in units of; and in.

Table E.2 lists percentile and median HCN/CO and SFR/HCN values for centre and discs environments discussed in Sec. 3.3.

Table E.1. Galaxy sample (EMPIRE + ALMOND)

Galaxy (1)	R.A. (J2000) (2)	Dec. (J2000) (3)	d (Mpc) (4)	i (°) (5)	$\log_{10} M_*$ (M_\odot) (6)	$\log_{10} \text{SFR}$ ($M_\odot \text{ yr}^{-1}$) (7)	$\log_{10} (\text{SFR}/M_*)$ (yr^{-1}) (8)	Bar (9)	AGN (10)	SFR tracer (11)	H I survey (12)	CO survey (13)	HCN survey (14)	HCN resolution ($''$) (15)	HCN resolution (kpc) (16)
NGC 0628	1 ^h 36 ^m 41.725 ^s	15°47'11.148"	9.84	8.90	10.34	0.24	-10.10	×	×	W4+FUV	THINGS	PHANGS-ALMA	ALMOND	18.60	0.89
NGC 1097	2 ^h 46 ^m 18.949 68 ^s	-30°16'28.83"	13.58	48.60	10.76	0.68	-10.08	✓	✓	W4+FUV	PHANGS-MeerKAT	PHANGS-ALMA	ALMOND	19.40	1.28
NGC 1365	3 ^h 33 ^m 36.364 ^s	-36°8'25.454"	19.57	55.40	10.99	1.23	-9.76	✓	✓	W4+FUV	×	PHANGS-ALMA	ALMOND	20.60	1.95
NGC 1385	3 ^h 37 ^m 28.563 ^s	-24°30'4.183"	17.22	44.00	9.98	0.32	-9.66	×	×	W4+FUV	PHANGS-VLA	PHANGS-ALMA	ALMOND	19.90	1.66
NGC 1511	3 ^h 59 ^m 36.590 ^s	-67°38'2.148"	15.28	72.70	9.91	0.36	-9.55	×	×	W4+FUV	PHANGS-MeerKAT	PHANGS-ALMA	ALMOND	17.60	1.30
NGC 1546	4 ^h 12 ^m 36.292 ^s	-56°3'39.232"	17.69	70.30	10.35	-0.08	-10.43	×	×	W4+FUV	×	PHANGS-ALMA	ALMOND	18.90	1.62
NGC 1566	4 ^h 20 ^m 0.381 ^s	-54°56'16.836"	17.69	29.50	10.78	0.66	-10.13	✓	✓	W4+FUV	MHONGOOSE	PHANGS-ALMA	ALMOND	19.70	1.69
NGC 1672	4 ^h 45 ^m 42.489 ^s	-59°14'50.125"	19.40	42.60	10.73	0.88	-9.85	✓	✓	W4+FUV	MHONGOOSE	PHANGS-ALMA	ALMOND	18.20	1.71
NGC 1792	5 ^h 5 ^m 14.325 ^s	-37°58'50.016"	16.20	65.10	10.61	0.57	-10.04	×	×	W4+FUV	×	PHANGS-ALMA	ALMOND	18.70	1.47
NGC 2566	8 ^h 18 ^m 45.607 ^s	-25°29'58.272"	23.44	48.50	10.71	0.94	-10.15	✓	×	W4	PHANGS-VLA	PHANGS-ALMA	ALMOND	18.50	2.10
NGC 2903	9 ^h 32 ^m 10.106 ^s	21°30'3.0276"	10.00	66.80	10.63	0.49	-10.15	×	×	W4+FUV	THINGS	PHANGS-ALMA	ALMOND	18.30	0.89
NGC 2997	9 ^h 45 ^m 38.793 ^s	-31°11'27.924"	14.06	33.00	10.73	0.64	-10.09	×	×	W4+FUV	PHANGS-VLA	PHANGS-ALMA	ALMOND	20.40	1.39
NGC 3059	9 ^h 50 ^m 8.16 ^s	-73°55'19.902"	20.23	29.40	10.38	0.38	-10.00	✓	×	W4	PHANGS-MeerKAT	PHANGS-ALMA	ALMOND	16.70	1.64
NGC 3184	10 ^h 18 ^m 16.941 ^s	41°25'27.6348"	12.58	16.00	10.36	0.11	-10.24	✓	✓	W4+FUV	THINGS	EMPIRE	EMPIRE	33.30	2.03
NGC 3521	11 ^h 5 ^m 48.576 ^s	0°2'9.4164"	13.24	68.80	11.02	0.57	-10.45	×	×	W4	THINGS	PHANGS-ALMA	ALMOND	21.10	1.35
NGC 3621	11 ^h 18 ^m 16.300 ^s	-32°48'45.36"	7.06	65.80	10.06	-0.00	-10.06	×	✓	W4+FUV	THINGS	PHANGS-ALMA	ALMOND	18.90	0.65
NGC 3627	11 ^h 20 ^m 15.004 ^s	12°59'29.4"	11.32	57.30	10.83	0.58	-10.25	✓	✓	W4+FUV	THINGS	EMPIRE	EMPIRE	33.30	1.83
NGC 4254	12 ^h 18 ^m 49.632 ^s	14°24'59.0832"	13.10	34.50	10.42	0.49	-9.94	×	×	W4+FUV	VLA-HERACLES	EMPIRE	EMPIRE	33.30	2.11
NGC 4303	12 ^h 21 ^m 54.931 ^s	4°28'25.4784"	16.99	23.50	10.52	0.73	-9.80	✓	✓	W4+FUV	PHANGS-VLA	PHANGS-ALMA	ALMOND	20.20	1.66
NGC 4321	12 ^h 22 ^m 54.928 ^s	15°49'20.2944"	15.21	38.50	10.75	0.55	-10.19	✓	✓	W4+FUV	VLA-HERACLES	PHANGS-ALMA	ALMOND	19.60	1.45
NGC 4535	12 ^h 34 ^m 20.304 ^s	8°11'52.7028"	15.77	44.70	10.53	0.33	-10.20	✓	×	W4+FUV	PHANGS-MeerKAT	PHANGS-ALMA	ALMOND	22.80	1.74
NGC 4536	12 ^h 34 ^m 27.067 ^s	2°11'17.6748"	16.25	66.00	10.40	0.54	-9.86	✓	×	W4+FUV	VLA-HERACLES	PHANGS-ALMA	ALMOND	21.50	1.69
NGC 4569	12 ^h 36 ^m 49.824 ^s	13°9'46.35"	15.76	70.00	10.81	0.12	-10.68	✓	✓	W4+FUV	VIVA	PHANGS-ALMA	ALMOND	19.20	1.47
NGC 4826	12 ^h 56 ^m 43.641 ^s	21°40'59.0988"	4.41	59.10	10.24	-0.69	-10.93	×	✓	W4+FUV	THINGS	PHANGS-ALMA	ALMOND	18.70	0.40
NGC 5055	13 ^h 15 ^m 49.296 ^s	42°1'45.4008"	9.02	59.00	10.79	0.31	-10.48	×	×	W4+FUV	THINGS	EMPIRE	EMPIRE	33.30	1.46
NGC 5194	13 ^h 29 ^m 52.689 ^s	47°11'42.5472"	8.56	21.00	10.65	0.64	-10.01	×	✓	W4+FUV	THINGS	PAWS	EMPIRE	33.30	1.38
NGC 5248	13 ^h 37 ^m 32.006 ^s	8°53'6.702"	14.87	47.40	10.41	0.36	-10.05	✓	×	W4+FUV	PHANGS-VLA	PHANGS-ALMA	ALMOND	19.90	1.43
NGC 5643	14 ^h 32 ^m 40.776 ^s	-44°10'28.596"	12.68	29.90	10.34	0.41	-9.92	✓	✓	W4	×	PHANGS-ALMA	ALMOND	18.00	1.11
NGC 6300	17 ^h 16 ^m 59.472 ^s	-62°49'13.98"	11.58	49.60	10.47	0.28	-10.19	✓	✓	W4	×	PHANGS-ALMA	ALMOND	17.70	0.99
NGC 6946	20 ^h 34 ^m 52.603 ^s	60°9'12.654"	7.34	33.00	10.47	0.77	-9.70	✓	×	W4+FUV	THINGS	EMPIRE	EMPIRE	33.30	1.18
NGC 7496	23 ^h 09 ^m 47.284 ^s	-43°25'40.26"	18.72	35.90	10.00	0.35	-9.64	✓	✓	W4+FUV	PHANGS-MeerKAT	PHANGS-ALMA	ALMOND	17.90	1.62

Notes – (2) Right ascension, (3) declination, (4) distance (Anand et al. 2021), and (5) inclination angle (Lang et al. 2020). Integrated galaxy properties, (6) global stellar mass and (7) global star formation rate, taken from Leroy et al. (2019). (9) Presence of a galactic bar (Herrera-Endoqui et al. 2015; Querejeta et al. 2021), and/or (10) active galactic nucleus (Veron-Cetty & Veron 2010). (11) Employed SFR tracers using WISE 22 μm (Wright et al. 2010) or a combination of WISE and GALEX-FUV (Martin et al. 2005), adopted from (Leroy et al. 2019). (12) Archival H I 21-cm line emission data, taken from THINGS (Walter et al. 2008), VIVA (Chung et al. 2009), VLA-HERACLES, PHANGS-VLA (Utomo et al. in prep.), PHANGS-MeerKAT (Eibensteiner et al. 2024, ; Pisano et al. in prep.), and MHONGOOSE (de Blok et al. 2024). (13) Archival CO observations from PHANGS-ALMA (CO(2 – 1); Leroy et al. 2021b) for ALMOND galaxies, and EMPIRE (CO(1 – 0); Jiménez-Donaire et al. 2019), PAWS (CO(1 – 0); Schinnerer et al. 2013) for EMPIRE galaxies. (14) Adopted HCN data from ALMOND (Neumann et al. 2023b) and EMPIRE (Jiménez-Donaire et al. 2019). (15) HCN native angular resolution and (16) corresponding linear resolution, given the distance d .

Table E.2. Galaxy centres vs. discs

$\log_{10}(Y)$	environment	(16 th , 50 th , 84 th) perc. ($S/N \geq 3$)	median (all S/N)
HCN/CO	disc	(-1.96, -1.72, -1.51)	-1.87
	centre	(-1.60, -1.35, -1.04)	-1.35
	centre (AGN)	(-1.43, -1.30, -1.03)	-1.28
	centre (non-AGN)	(-1.62, -1.43, -1.22)	-1.43
SFR/HCN	disc	(-7.21, -6.93, -6.56)	-6.85
	centre	(-7.39, -7.13, -6.57)	-7.11
	centre (AGN)	(-7.44, -7.19, -6.70)	-7.23
	centre (non-AGN)	(-7.31, -7.11, -6.57)	-7.11

Notes – 16th percentiles, medians, and 84th percentiles of HCN/CO and SFR/HCN across significant data ($S/N \geq 3$) in disc and centre environments. For the centres, we also present percentile values among centres with and without AGNs. The last column additionally lists the median values across all S/N data, this means including non-detections, which yields 0.15 dex lower HCN/CO and 0.08 dex higher SFR/HCN across galaxy discs, which are affected by S/N -clipping (and similar values in centres, which have $S/N \geq 3$ for 29 out of 31 galaxies).

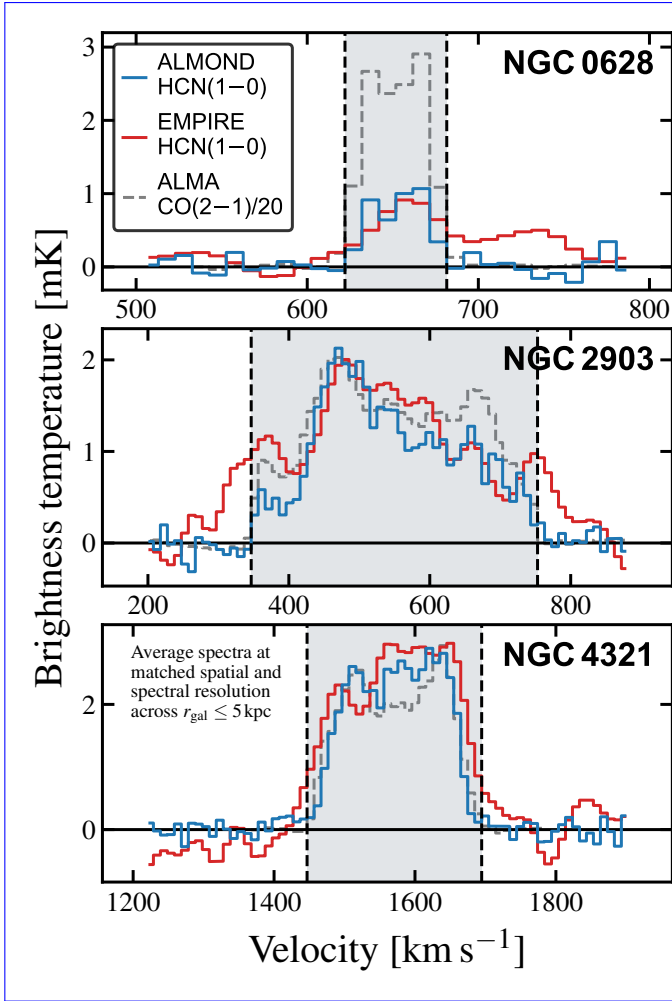


Fig. D.1. EMPIRE versus ALMOND: HCN(1 – 0) average spectra. The blue and red lines show average HCN brightness temperatures within $r_{\text{gal}} \leq 5$ kpc obtained from spatially and spectrally matched ALMOND and EMPIRE observations, respectively, across the three galaxies NGC 628, NGC 2903, NGC 4321 from top to bottom. The grey dashed line shows (homogenised) CO(2 – 1) intensities from PHANGS–ALMA (Leroy et al. 2021b), scaled down by a factor of 20. The grey-shaded area indicates the velocity-integration window constructed using the highly significant CO(2 – 1) data. The resulting integrated intensities are quoted in the text.

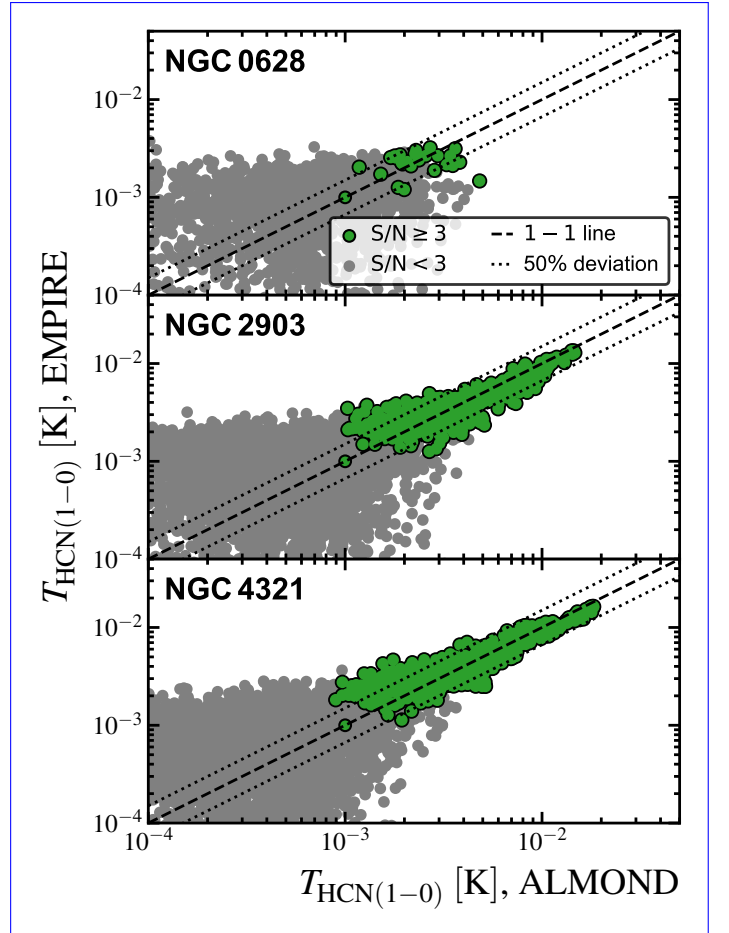


Fig. D.2. EMPIRE versus ALMOND: HCN(1 – 0) brightness temperature. Green data points present data, where EMPIRE and ALMOND both yield a 3-sigma detection. Grey data shows low-significant data points. The dashed line marks the 1-to-1 relation, where the dotted lines indicate a $\pm 50\%$ deviation.

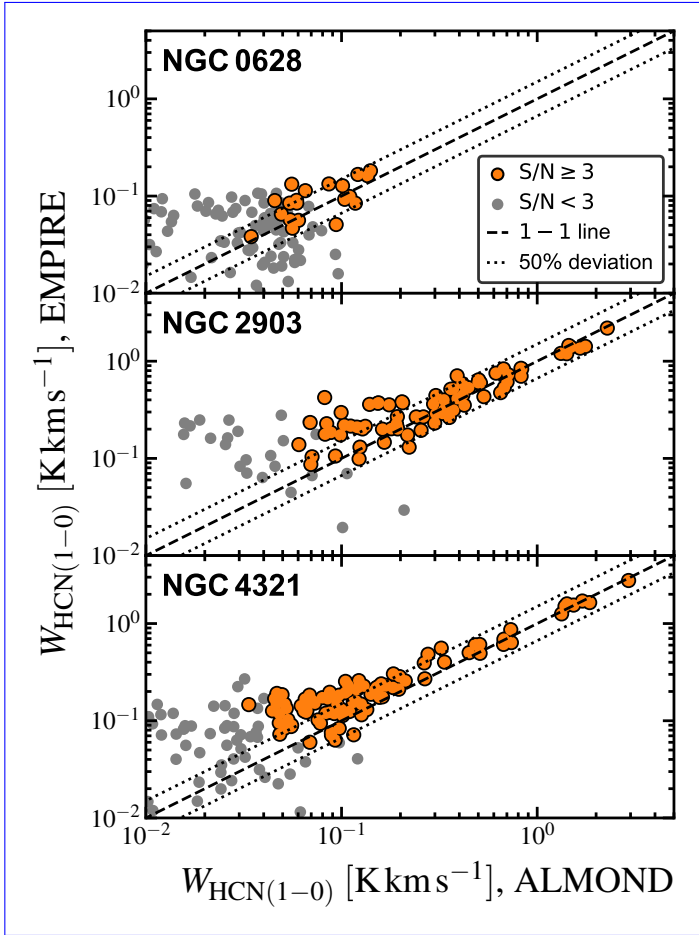


Fig. D.3. EMPIRE versus ALMOND: HCN(1 – 0) integrated intensity. Similar to Fig. D.2, but showing the integrated intensities (moment-0) computed across a CO-inferred velocity integration window. Orange and grey points denote data above and below 3-sigma, respectively.

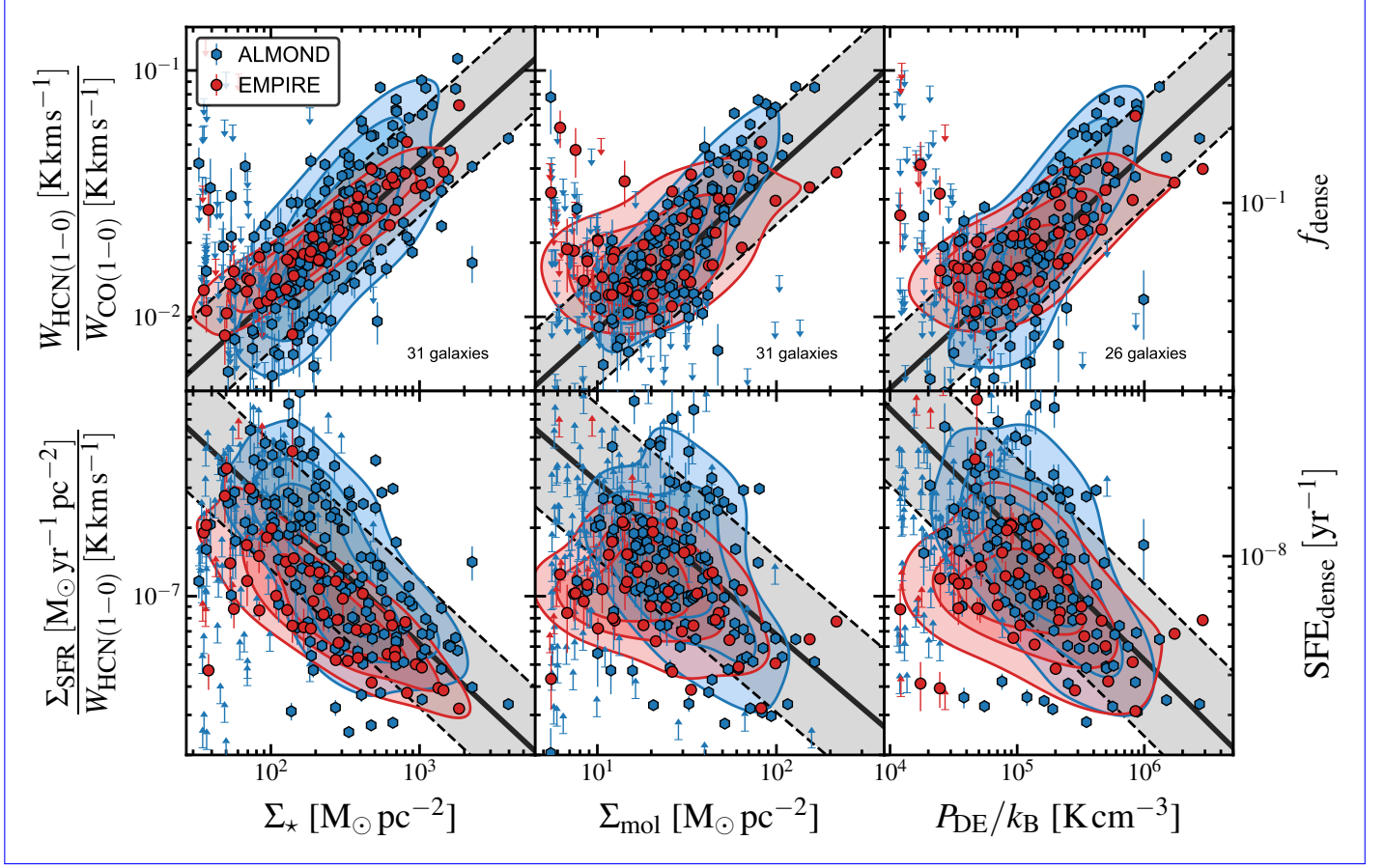


Fig. D.4. Similar to Fig. 3, but separately showing kiloparsec-scale, stacked measurements from ALMOND (blue hexagons) and EMPIRE (red circles). The best-fit line (solid black line) and the corresponding 1-sigma scatter (grey-shaded area) are computed from the combined data using LinMix.